

Partially graphitized Iron-carbon hybrid composite as electrochemical supercapacitor material

Sai Rashmi Manippady,^[a] Ashish Singh,^[b] Chandra Sekhar Rout,^[a] Akshaya Kumar Samal,^[a] and Manav Saxena^{*[a]}

[a] Ms. S. R. Manippady, Dr. C. S. Rout, Dr. A. K. Samal, Dr. M. Saxena
Centre for Nano and Material Sciences
Jain University
Ramanagra, Bangalore-562112, Karnataka, India
E-mail: manavsaxena19@gmail.com, s.manav@jainuniversity.ac.in (MS)

[b] Dr. A. Singh
Department of Chemistry
Indian Institute of Technology Kanpur
Kanpur, Uttar Pradesh-208016, India

Abstract: The conversion of biomass into valuable carbon composites as an efficient non-precious energy storage electrode material has elicited extensive research interests. As synthesized partially graphitized iron oxide-carbon composite material ($\text{Fe}_3\text{O}_4/\text{Fe}_3\text{C}@C$) shows an excellent property as an electrode material for supercapacitor. X-ray diffraction analysis, high resolution transmission electron microscopy, X-ray photo-electron spectroscopy and Brunauer-Emmett-Teller analysis is used to study the structural, compositional and surface areal properties. The electrode material shows a specific surface area of $827.4 \text{ m}^2/\text{g}$. Due to the synergistic effect of graphitic layers with iron oxide/carbide, $\text{Fe}_3\text{O}_4/\text{Fe}_3\text{C}@C$ hybrid electrode materials display high-performance for supercapacitor with excellent capacity of 878 F/g at a current density of 5 A/g (3-electrode) and 211.6 F/g at a current density of 0.4 A/g (2-electrode) in 6 M KOH electrolyte with good cyclic stability.

Introduction

The large percentage of energy consumed globally is generated from non-renewable fossil fuels. Although alleviating carbon emission is a multifaceted challenge, the cardinal of the future low-carbon economy will substantially dependent on renewable energy sources and storage systems. The ever-growing energy demand has stimulated intense research on economic, alternative energy storage systems with high efficiency and environmental benignity.^[1] Electrical energy from the renewable energy sources must be efficiently stored for on-demand utilization.^[2] In this scenario, electrochemistry provides a link for efficient inter-transfer of chemical to electrical energy.^[1a] Electrochemically active mesoporous materials are particularly advantageous for applications in energy storage owing to their high surface areas and large pore volumes.

In the field of mesoporous materials, carbon-based functional materials represent the most investigated electrode materials for energy storage applications due to their excellent electrochemical activity as well as other advantages, including low costs and environmental friendliness.¹ A gazillions of strategies have been attempted by choosing different precursors to design supercapacitor with pseudocapacitive electrodes of carbon and oxides of iron,^[3] manganese,^[4] cobalt,^[5] vanadium,^[6] ruthenium,^[7] tungsten,^[8] nickel,^[9] and mixed metals^[10] for the enhanced electrochemical properties.^[3a] For carbon composites

synthesis chemistry, activating agents (e.g ZnCl_2 , KOH , H_3PO_4 , K_2CO_3) are used to enhance the surface area, unique porosities and activity which add few extra steps in the synthesis procedure. Among different transition metal, being abundant, low cost and having high theoretical capacitance,^[11] oxides of iron have gained widespread attentions and explored as an electrode material due to multiple valence states, rich redox pairs. The positive synergic coupling effects between the $\text{Fe}_x\text{O}_y\text{H}_z$ and carbon are superintended for its superior properties related to the energy storage applications.^[12] Polypyrrole/ Fe_2O_3 composite material by Xu et al. display gravimetric capacitance of 560 Fg^{-1} at current density of 5 Ag^{-1} measured by three-electrode system while using $0.5 \text{ M Na}_2\text{SO}_4$ aqueous solution as electrolyte.^[3a] Fe_2O_3 nanoparticles decorated on graphene-carbon nanotubes display gravimetric capacitance of 675 Fg^{-1} at 1 Ag^{-1} measured by three-electrode system in 6 M KOH electrolyte.^[3b] Rudra et al. reported Au- Fe_2O_3 composite nanorods having gravimetric capacitance of $\sim 570 \text{ Fg}^{-1}$ at 1 A g^{-1} in $0.5 \text{ M aq. H}_2\text{SO}_4$ in a three-electrode system.^[3c] Ishaq et al. reported 232 Fg^{-1} gravimetric capacitance of ternary composite rGO/ MnFe_2O_4 /polypyrrole electrode measured by two-electrode system in $1 \text{ M H}_2\text{SO}_4$.^[13] Zhou. et al. reported gravimetric capacitance of 1116.6 Fg^{-1} at 10 Ag^{-1} current density in $1 \text{ M aq. Na}_2\text{SO}_4$ for spindle-like carbon incorporated- Fe_2O_3 grown on carbon nanotube fiber in a three-electrode system.^[10a]

Recently, the carbon derived from biomass especially biowaste, has sparked tremendous interest in the energy related material research. The potential candidacy of the biowaste derived carbon is primarily due to the inexpensiveness, sustainability, abundance, and environmental friendliness of the raw materials, as well as the high performance of the resultant carbon.

In the present study, we demonstrate a simple and effective strategy to synthesize the iron-carbon-based functional material, the composite of sustainable bagasse (*Saccharum officinarum*) and iron oxide/carbide. Notably, bagasse is a waste biomass (dry fibrous residue) that remains after sugarcane stalks are crushed to extract their juice with a composition of 32-34% cellulose, 19-24% hemicellulose, 25-32% lignin, 6-12% extractives and 2-6% ash.^[14] The cane juice comprises mainly of sugar (sucrose) 9-12% (w/v).^[15] Herein, we apply the high compatibility and coordinating capability of oxygen-containing groups (methoxy, carboxyl and phenolic) in bagasse with Fe^{3+} ions^[16] and realize the uniform

distribution of iron oxide particles in the carbon matrix during the carbonization process. Benefiting from the synergistic effect of structure and component, the iron oxide doped partially graphitized carbon composite displays high-performance as $\text{Fe}_3\text{O}_4/\text{Fe}_3\text{C}@C$ hybrid electrode materials for supercapacitor with excellent capacity and rate capabilities in alkaline media.

Results and Discussion

Coordination of Fe^{3+} ions with oxygen functional groups present in the bagasse (methoxy, carboxyl, phenolic) from sugar, lignin moieties allows homogenous distribution of Fe^{3+} ions [16] and thus during carbonization, iron oxide particles uniformly embedded in the carbon matrix. The synthesis scheme and probable mechanism of graphitization is shown in Figure 1.

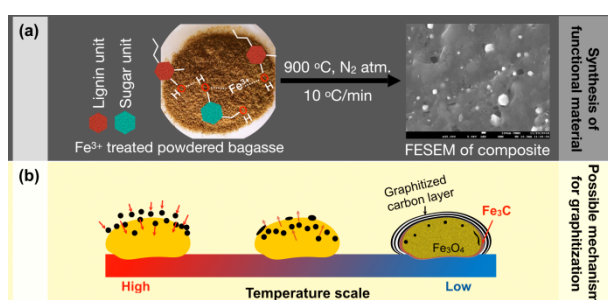


Figure 1: Schematic representation for (a) Synthesis of functional composite material, (b) Possible mechanism for graphitization and Fe_3C formation.

The crystallographic structure of the CF0 and CF10 were analyzed using PXRD pattern. The PXRD pattern of CF0 shows the broad peak at $2\theta = 23.3^\circ$ and 43.8° refers to the (002) and (100) plane of carbon, and indicates the amorphous nature of the carbon (Figure S1).^[17] PXRD of CF10 shows sharp peaks suggesting the crystalline nature/crystallites in the material (Figure 2a). The distinct diffraction PXRD peaks of CF10 at $2\theta = (30.18, 35.57, 43.18, 53.68, 57.23, 62.87, 71.27, 74.16$ and $79.15)^\circ$ corresponds to the (022), (131), (040), (242), (151), (044), (062), (353) and (444) crystal planes of the Fe_3O_4 (ref. code 96-900-5839). The diffraction peaks at $2\theta = (43.6, 50.79$ and $74.82)^\circ$ corresponds to the (111), (020) and (022) of Fe (ref. code 96-900-8470) respectively. Moreover, the peak at $2\theta: 44.68^\circ$ correspond to the (031) crystal plane of the Fe_3C (ref. code 96-901-6232). The characteristic peaks for carbon, Fe, Fe_3O_4 and Fe_3C suggesting the coexistence of Fe, Fe_3O_4 , Fe_3C and carbon in the hybrid networks $\text{Fe}_3\text{O}_4/\text{Fe}_3\text{C}@C$ which is also supported by HRTEM.

The chemical compositions and valence states of the CF0 and CF10 composites were analyzed by X-ray photoelectron spectroscopy (XPS) (Figure 2b, S2). The high-resolution Fe2p spectrum of CF-0 confirms the absence of iron species in CF0 (Figure S2). Figure 2b shows the high-resolution Fe2p spectrum of CF10. The broad peak centered at 708.3 eV is assigned as a merged peak for Fe(II) $2p_{3/2}$ and Fe_3C (Fe-C).^{[18] [19] [20]} The peak at 711.8 eV is corresponding to Fe(III) $2p_{3/2}$. Based on the above discussion, the presence of Fe_3O_4 and Fe_3C could be concluded in the CF10. The Fe-concentration quantified in the CF0 and CF10 is 0 and 1.4 at.% respectively (Table S1).

Comparative Raman spectra of CF0 and CF10 are shown in Figure 2c. The G band for CF0 and CF10 are positioned at 1607 and 1589 cm^{-1} respectively. The FWHM of G-band of CF0 and CF10 is $\sim 100.6 \text{ cm}^{-1}$ which is much higher than the crystalline graphite. The D band of CF0 and CF10 is positioned at 1349 cm^{-1} . The FWHM of D-band of CF10 is 125.7 cm^{-1} as compared to 176.1 cm^{-1} of CF0. The decrease in the FWHM of D-band is due to the formation of ordered structure and thus suggests the presence of partial graphitized structure. A new peak at 2680 cm^{-1} corresponding to 2D band that arises in CF10 confirms the presence of graphitized carbon structure which is absent in CF0. The graphitization of CF10 is also consistent with HRTEM and PXRD analysis.

The adsorption-desorption curves of CF0, CF10 and CF20 (Figure 2d and S3) were ascribed to typical type I (CF0) and type IV (CF10, CF20) profiles. The specific surface area (SSA) of CF10 is $\sim 828 \text{ m}^2\text{g}^{-1}$ which is $\sim 12\%$ higher than the CF0 ($\sim 740 \text{ m}^2\text{g}^{-1}$). The detailed textural properties are tabulated in Table S1. The pore size distribution (PSD) of CF10 reveals that the ratio of mesopores to micropores is 0.26, 1.24, and 2.3 for CF0, CF10 and CF20 respectively (Table S2). The ratio suggest that with increase in iron content the mesopores formation is preferred. The pore size distribution (PSD) for CF10 showed the pore diameters are in the range (1.2-1.5 nm) and (2.9-5.2 nm) respectively.^[21] The SSA of CF20 is $\sim 190 \text{ m}^2\text{g}^{-1}$ which is lesser than CF0 and CF10 (Figure S3b). The decrease in CF20 SSA might be due to higher loading of iron oxide which occupied the void and surface space in the layered material.^[22]

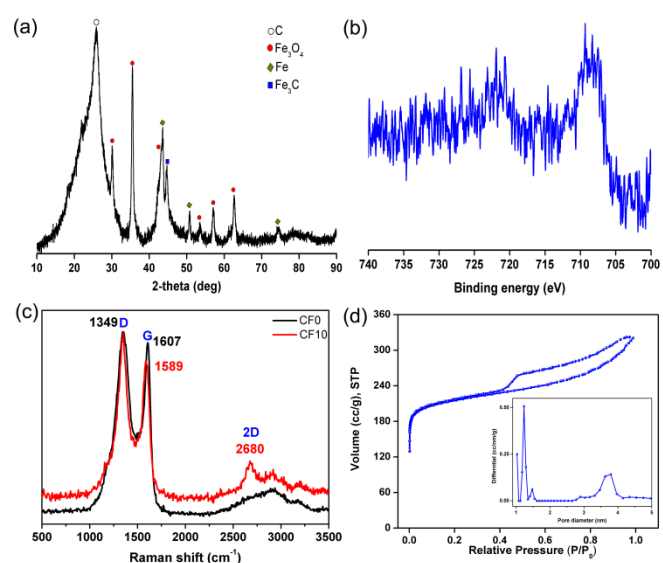


Figure 2: (a) PXRD, (b) Fe2p XPS spectrum, (c) Raman spectra of CF0, CF10, (d) N_2 adsorption-desorption isotherms, inset: pore size distribution of CF10.

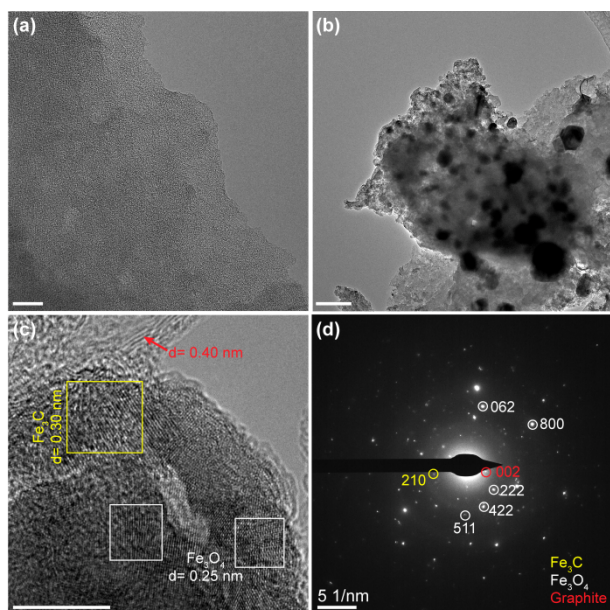


Figure 3: HRTEM images of (a) CF0, (b-c) CF10, (d) SAED of CF10. Scale bar: (a) 20 nm, (b) 200 nm, (c) 10 nm, (d) 5 1/nm.

Surface morphology of the control (CF0), CF10 and CF20 are analyzed through HRTEM. HRTEM reveals that CF-0 contains porous layered carbon structure (Figure 3a). The absence of graphitized layers indicates that CF0 is amorphous in nature which is also supported by PXRD data (Figure S1). CF10 composite shows partial graphitized structures located around the polydisperse masses of Fe₃O₄/Fe₃C distributed throughout the layered carbon structure (Figure 3b). The d-spacing of 2.5 Å (white squares, Figure 3c, S4a) matches to the (131) crystal plane of Fe₃O₄ (ref. code: 96-900-5839) which is also supported by PXRD ($2\theta=35.57^\circ$). The d-spacing of 3.0 Å (yellow square, Figure 3c, S4b), corresponds to the (111) crystal plane of Fe₃C (ref. code: 96-901-6232). The formation of Fe₃C is interesting and might be due to the high solubility of carbon in the iron. The solubility of carbon in Fe is temperature-dependent and show higher solubility ~7.0 at.% at 1000 °C. At higher temperatures, the Fe³⁺ ions convert to Fe₃O₄ or Fe by carbon reduction and simultaneously carbon diffuses into the iron oxide particles. The temperature dependency leads to the carbon segregation from the bulk during cooling and catalyzed the growth of graphitized structure and iron carbide (Figure 1b).^[23] The graphitized structures along the particles are detected having interlayer spacing of 4 Å (marked with red arrow, Figure 3c). The iron content in CF0 and CF10 is further quantified using energy dispersive X-ray spectroscopy (EDS) during TEM analysis. The atomic percentage of Fe quantified in CF0 and CF10 are 0 and 1.6% respectively (Table S1) which is closer to 1.4 at.% obtained from XPS. The amount of oxygen increases from 2 (CF0) to 5 (CF10) at.% in presence of iron. The oxygen groups from lignin, sugar covalently bonded with iron and thus upon carbonization more oxygen retains with CF10 which is in well agreement with EDS and XPS analysis (Table S1).

The grown graphitized structures are detected and show 4.0 Å interlayer spacing corresponds to (002) plane which is also in well agreement with $(d=3.8 \text{ \AA})_{2\theta=23.3^\circ}$ calculated from PXRD. Selected area electron diffraction (SAED) pattern of CF10 shows

characteristic diffraction spots for different planes of Fe₃O₄, Fe₃C and graphitized carbon and thus confirms the formation of Fe₃O₄/Fe₃C@C composite (Figure 3d). The CF20 composite also shows the layered structure impregnated with iron oxide nanoparticles similar to CF10 (Figure S5).

Electrochemical performance of Carbon-iron composite:

3-electrode system: The electrochemical performance of the CF0, CF10, CF20 and bare Ni foam is measured by cyclic voltammetry (CV) at a scan rate of 100 mV/s (Figure 4a). The materials show a pseudocapacitive behavior via redox couple of Fe²⁺/Fe³⁺ with an oxidation and reduction peaks. The CV curves of the bare Ni foam, CF0, CF20 at the 100 mV/s scan rate show the lesser area as compared to the CF10. A smaller area suggests the smaller value of C_{sp} for bare Ni foam, CF0 and CF20 as compared to CF10 as C_{sp} is directly related to the area under the CV curve. On the basis of above discussion, it could be concluded that CF10 has the best capacitive performance. The electrochemical performance of CF10 was studied by CV curves at different scan rates of 5, 10, 40, 80 and 100 mV/s (Figure 4b). The specific capacitance is measured using equation 1. CF10 shows 443.3, 412.2, 259.7, 180.6 and 158.1 F/g specific capacitance at 5, 10, 40, 80 and 100 mV/s scan rate respectively which is ~three times higher than CF0 (141.3 F/g), and CF20 (230.8 F/g) at 5 mV/s (Figure S6, Table S3). This outstanding electrochemical performance and large area for CF10 composite may be due to the synergistic interaction between the Fe₃O₄/Fe₃C nanoparticles with the carbon material.^[24] The highest specific capacitance is found to be for CF10 composite which has the optimal loading of Fe₃O₄/Fe₃C nanoparticles. Further increase in metal oxide loading (CF20) leads to decrease in the specific capacitance. Though it is proved that the decrease in surface area results in decreases in specific capacitance, another reason might be excess loading of the iron oxide which will lead to an overall decrease of active surface area for electrochemical reactions in the CF20, and results the decreases the specific capacitance.^[25] Further, GCD cycles are shown in Figure 4c and the specific capacitance is measured from the discharge curve using equation 2. The quasi-triangular shape of the charge-discharge curve indicates pseudocapacitive nature of the composite due to faradaic transformation.^[26] The specific capacitance for CF10 calculated from GCD is 878.0, 868.3, 863.1, 836.8 and 800 F/g at current densities of 5, 6, 7, 8 and 9 A/g respectively which is higher than CF0 and CF20 with C_{sp} of 25.7 F/g and 381.6 F/g at 5 A/g (Table S3) respectively. The C_{sp} of CF10 is higher than the reported results for Fe₃O₄@hollow graphite shells (481 F/g, 1 A/g),^[27] α-Fe₂O₃/rGO flexible electrode (714 F/g, 1 A/g),^[28] Fe₃O₄/rGO nanosheets hybrid (455 F/g, 3.6 A/g),^[29] and rGO/Fe₂O₃ composite (577.5 F/g, 2 A/g)^[30]. Figure 4d and 4e represent the specific capacitance as a function of scan rate and current density respectively. As the scan rate and current density increases, the specific capacitance displays a gradual attenuation from 443.3 F/g (at 5 mV/s) to 158.1 F/g (at 100 mV/s) with capacitance retention of ~36%. The increase in current density results in a decrease in C_{sp} due to the slow redox reaction rate at high current density.^[31] The decrease in specific capacitance is due to the diffusion limitation and underutilization of the active material at higher specific currents.^[32] The contribution of Ni foam substrate to the capacitances is found negligible. Importantly, for the application point of view, cyclic stability of an electrode material

plays a significant role. For CF10 composite, after 5000 charge-discharge cycles, C_{sp} is found to be 101.0 F/g (Figure 4f), which is ~84% of its initial capacitance after stabilization at 50 A/g current density. Also, the electrode material shows higher cyclic stability as compared to earlier reports.^[33] Hence, having good stability enables the material for its practical applicability.

Furthermore, the EIS is carried out to understand the capacitive and resistive behavior of CF10 and CF0 within the frequency range of 0.5 Hz to 100 kHz with 1 mV amplitude with an open circuit perturbation potential of 5 mV. In the Nyquist plot, high frequency is semicircle region indicating the charge transfer resistance (R_{ct}) and low-frequency area is the straight line indicating the diffusion of ions in electrode material.^[29] Nyquist plot with Randle's equivalent circuit (inset) depicted in Figure 4g shows that for CF10, the R_{ct} value is 1.77 Ω with less inclined line as compared to the CF0 with R_{ct} value of 2.85 Ω . The R_s value is found to be 0.92 Ω and 1.38 Ω for CF10 and CF0 respectively. The increase in R_{ct} value is due to the low charge transfer rate seen in control sample. Hence the high capacitance of CF10 results from the low equivalent series resistance.

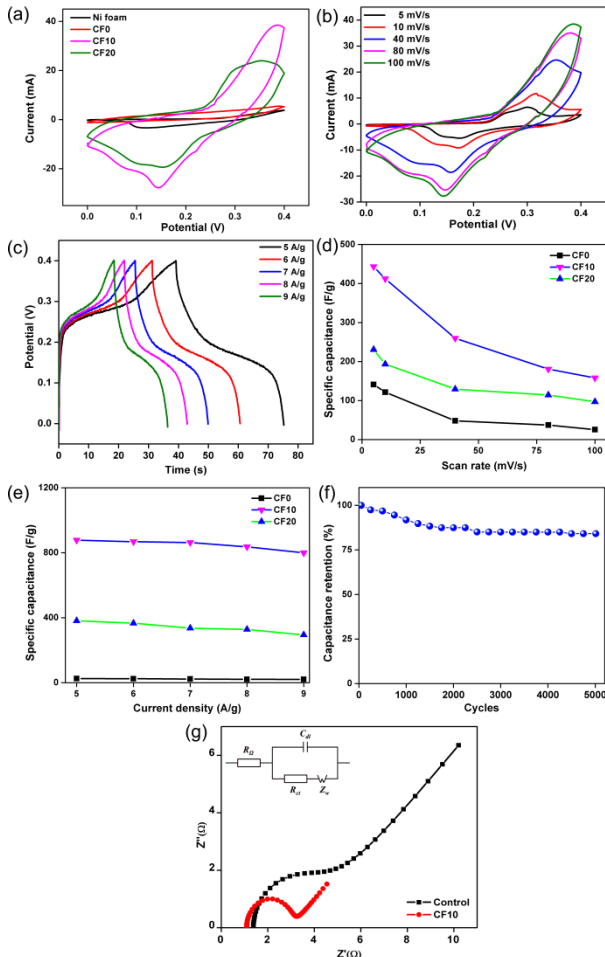


Figure 4: Electrochemical characterization. (a) CV curves at 100 mV/s for bare Ni foam, CF0, CF10 and CF20, (b) CV curves of CF10 at different scan rates, (c) Galvanostatic charge-discharge curves at different current densities for CF10, (d) Deviation in specific capacitance at different scan rate, (e) Deviation in specific capacitance at different current densities, (f) Cycling performance of the CF10 at 50 A/g current density, (g) EIS Nyquist plot for CF0 and CF10, inset showing equivalent circuit.

2-electrode system:

The CV curve obtained for the symmetric capacitor is measured using a potential window of 0-1 V at different sweep rates. The cyclic voltammetry of CF10 shows a more rectangular shape graph representing an ideal capacitive behavior, resulting in the low charge transfer resistance which further leads to better ion diffusion^[34] (Figure 5a). Figure 5a and 5b show the CV of CF10 at different scan rates and GCD plot at different discharge current densities respectively. The calculated specific capacitance values of CF10 from CV are 163.9, 161.5, 143.2 and 135.4 F/g at 40, 80, 100 and 200 mV/s scan rate respectively. The higher capacitance with a slower scan rate is due to the well interaction of electrolyte and the electrode material. Further, GCD curves depict almost triangular shape suggesting good columbic efficiency and electrochemical reversibility. The specific capacitances calculated from GCD curves are 211.6, 203.9, 197.5 and 193.8 F/g at 0.4, 0.7, 1 and 2.5 A/g respectively. The specific capacitance 163.9 F/g (40mV/s) and 211.6 F/g (0.4 A/g) of CF10 is higher than the recently reported value e.g. 169.5 F/g (0.5 A/g) using $Fe_2O_3/GNs/CNTs$ conductive networks,^[3b] 162.9 F/g (5mV/s) of $rGO/NiFe_2O_4/PPy$ ^[13], 182 F/g (2 A/g) of $CuCo_2O_4//G@Fe_3O_4$.^[3e] The specific energy of CF10 material is found to be 29.4 Wh/Kg, power density of 807 W/Kg. We have measured GCD cycles to understand the cyclic stability of the CF10 within the potential window of 1.0 V at a current density of 20 A g⁻¹ for 5000 cycles. Figure 5c shows the retention of specific capacitance for CF10 as a function of the cycle number. Interestingly, we observed that the CF10 show retention of ~94% of its specific capacitance after stabilization, which is higher than the earlier reports.^[33a, 35] The GCD curves of CF10 at 20 A/g discharge current densities after 1st, 100th, 500th, 1000th, 2000th, 3000th, 4000th and 5000th cycle confirm that CF10 has good stability (Figure 5d).

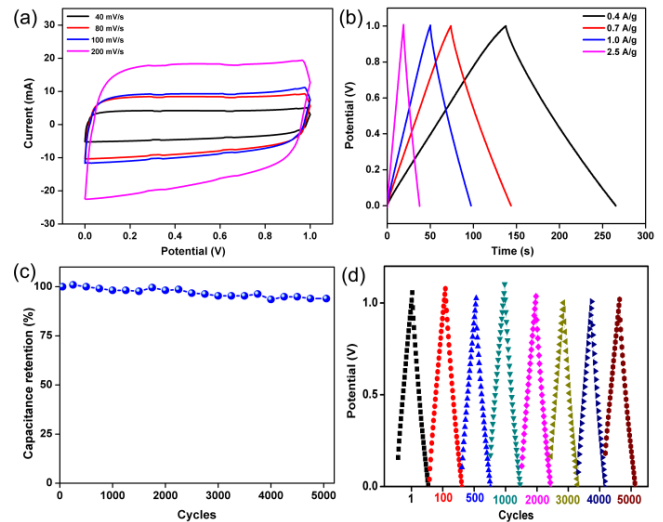


Figure 5: Electrochemical characterization of CF-10 (a) CV curves at different scan rate, (b) GCD curves at different current densities, (c) Cycling stability measurements of CF10 at 20 A/g current density, (d) Comparison of the GCD curves at 20 A/g after selected cycles.

Table 1. Comparison in specific capacitance of three and two electrode system with different material.

Electrode material	Specific capacitance ^[a]		Ref
	3-electrode	2-electrode	
Neem leaves derived carbon	400 F/g (0.5 A/g)	-	[17]
Fe ₂ O ₃ -poly(t-butyl acrylate)-block-polyacrylonitrile	235 F/g (0.5 A/g)	-	[21]
Recycled Jute derived carbon	185 F/g (0.5 A/g)	51 F/g (5 mV/s)	[36]
rGO/Fe ₃ O ₄ /PANI	631.7 F/g (1.0 A/g)	283.4 F/g (1 A/g)	[26a]
Fe ₃ O ₄ @Carbon Nanosheets	586.0 F/g (0.5 A/g)	58.5 F/g (1 A/g)	[35]
Fe Composite algal biochar	418.0 F/g (1 A/g)	368 F/g (1 A/g)	[22b]
Polypyrrole-Fe ₂ O ₃ nanohybrids	560.0 F/g (5A/g)	-	[3a]
Porous N-doped CNTs/Fe ₃ C	181.0 F/g (0.1A/g)	-	[37]
BiFeO ₃ nanowire-rGO nanocomposite	928.4 F/g (5A/g)	300 F/g (5A/g)	[10c]
Fe ₃ O ₄ particles coated with nitrogen-doped carbon	313.0 F/g (0.5 A/g)	-	[3d]
CNT-Fe ₃ O ₄ -PANI film	-	201 F/g (20 mV/s)	[38]
Sugar waste spent derived carbon	121.4 F/g (0.1 A/g)	105 F/g (0.2 A/g)	[39]
Porous Fe ₂ O ₃ nanocluster	357 F/g (10 mV/s)	-	[40]
Fe₃O₄-carbon composite	878.0 F/g (5 A/g)	211.6 F/g (0.4 A/g)	Present work

[a] Capacitance value in 3 and 2-electrode configuration at mentioned discharge current

Conclusion

A simple strategy toward synthesis of the carbon-based functional material (Fe₃O₄/Fe₃C@C) from bagasse and iron oxide is developed. By utilizing the high compatibility and coordinating capability of oxygen-containing groups of bagasse (from sugar and lignin moieties) with Fe³⁺, we have synthesized the composite having uniform distribution of iron oxide/carbide particles in the carbon matrix post carbonization. Due to the synergistic effect of graphitic layers with iron oxide/carbide, Fe₃O₄/Fe₃C@C hybrid electrode materials (CF10) display high-performance for supercapacitor with excellent capacity of 878 F/g at a current density of 5A/g (3-electrode) and 211.6 F/g at a current density of 0.4A/g (2-electrode) in 6M KOH electrolyte with good cyclic stability.

Experimental Section

Synthesis of the composite material

5g of powdered bagasse (< 50 μm) was soaked in 20 mL Fe(NO₃)₃.9H₂O solution, and kept for 24 h. Two samples prepared by choosing 10 and 20% (wt%) of Fe-precursor (w.r.t. bagasse weight) were dried in hot air

oven at 60 °C for 12h. The wt% of iron used will be 1.38 and 2.76% respectively. The iron treated bagasse was carbonization at 900 °C (heating rate of 10 °C/min) in a quartz tube furnace under a continuous flow of N₂ gas at 1 atm pressure. The furnace temperature was maintained at 900 °C for 1h and then cooled down to RT under N₂ flow. The control sample was also synthesized without Fe-precursor and referred to **CF0**. The iron-treated samples were referred to **CF10** and **CF20**, where the number (10, 20) represents the weight percentage of iron precursor Fe(NO₃)₃.9H₂O used as mentioned above.

Material Characterization

Nitrogen sorption isotherms were recorded at 77 K using Brunauer-Emmett-Teller (BET), surface area analyzer (Bellsorp Max, Japan). Based on the Barrett-Joyner-Halenda (BJH) model, pore size distribution plots were recorded from the desorption isotherms. Prior to the measurement, the samples were degassed at 200 °C under vacuum for 12 h. Powder X-ray diffraction (PXRD) (Rigaku X-ray diffraction ultima-IV, Japan) was recorded over a range of 5° to 90° with a scan speed of 1 deg/min using Cu-K_α radiation. The Surface morphology of the samples was studied using Thermo Scientific™ Talos™ F200S High-Resolution Transmission Electron Microscope (HRTEM). X-ray photoelectron spectroscopic (XPS) characterization was performed by PHI 5000 Versa ProBII, FEI Inc. Raman spectra was recorded using Horiba Jobin Yvon Xplora Plus V1.2 Multiline with 532 nm excitation wavelength.

Electrochemical Characterization:

Cyclic voltammetry (CV), Galvanostatic charge-discharge (GCD) and electrochemical impedance spectroscopy (EIS) were done using CHI660D potentiostat (CH instruments, Austin, USA).

3-electrode system: To carry out the electrochemical measurements, the synthesized hybrid materials were used as the working electrode, platinum wire as the counter electrode and Ag/AgCl (sat. KCl) as reference electrode. The working electrode material was prepared by mixing sample, super-p conducting carbon and polyvinylidene difluoride (PVDF) in a weight ratio of 80:10:10 in N-methyl-2-pyrrolidone (NMP) solvent. 1 mg active material was coated on the cleaned Ni-foam substrate in 0.8 cm² area and used as a working electrode. These electrodes were then dried in an oven for 12 h at 60 °C and then kept in vacuum desiccators for 2 h. The dried electrode substrates were compressed using a hydraulic press (pressure of ~5 tons). Further, the electrochemical studies were carried out using 6 M KOH solution as an electrolyte. The specific capacitance was calculated from CV and GCD were using by following equation (1) and (2) respectively.^[6]

2-electrode system:

The prepared slurry (2.5 mg) was coated on one side of two circular Ni-foams of diameter 1 cm. The modified nickel foams were dried in an oven at 60 °C for 12 h and kept in vacuum desiccators for 2 h. Whatman paper dipped in 6M KOH was used as a separator during device fabrication using a Swagelok system made from stainless steel. The specific capacitance in two-electrode systems was calculated from CV and GCD using equation (3) and (4) respectively. ^[6]

$$C_{sp} = 2[m_s(V_a - V_b)]^{-1} \int I(V) dV \quad (1)$$

$$C_{sp} = It/[m(V_a - V_b)] \quad (2)$$

$$C_{sp} = [m_s(V_a - V_b)]^{-1} \int 2[I(V) dV] \quad (3)$$

$$C_{sp} = 4 It/[m(V_a - V_b)] \quad (4)$$

where C_{sp} (F/g) denotes the specific capacitance, area under the CV curve is the integral part represented in the numerator, 'm' is the active mass of

the material deposited on the Nickel foam substrate, 's' is the scan rate and (V_a - V_b) is the working potential window. Further the energy and power density of the device were calculated using the equation (5) and (6) respectively.

$$E = \frac{1}{2} C \Delta V^2 \quad (5)$$

$$P = \frac{E}{\Delta t} \quad (6)$$

where E (Wh/kg) is the specific energy, ΔV is the potential window and P (W/Kg) is the specific power respectively.

Acknowledgements

SRM acknowledges Jain University for Junior Research fellowship. MS is grateful to the SERB, New Delhi, India for funding to conduct the research (EMR/2017/003368). The authors acknowledge Nanomission project (SR/NM/NS-20/2014) for FESEM & PXRD facilities. The authors acknowledge the TEM Facility, funded by a TPF Nanomission, Gol project and Raman characterization at Centre for Nano and Soft Matter Sciences, Bengaluru and Indian Institute of Technology Kanpur, India for XPS characterization.

Conflict of Interest

Authors declare no conflict of interest.

Author Contributions

All authors have given approval to the final version of the manuscript.

Keywords: Bagasse • supercapacitor • composite material • iron carbide • iron oxide

- [1] (a) Z.-L. Wang, D. Xu, H.-X. Zhong, J. Wang, F.-L. Meng, X.-B. Zhang, *Sci. Adv.* **2015**, *1*, e1400035; (b) W. Li, J. Liu, D. Zhao, *Nat. Rev. Mat.* **2016**, *1*, 16023.
- [2] Y. Shao, M. F. El-Kady, J. Sun, Y. Li, Q. Zhang, M. Zhu, H. Wang, B. Dunn, R. B. Kaner, *Chem. Rev.* **2018**, *118*, 9233-9280.
- [3] (a) C. Xu, A. R. Puente-Santiago, D. Rodríguez-Padrón, A. Caballero, A. M. Balu, A. A. Romero, M. J. Muñoz-Batista, R. Luque, *ACS Appl. Energy Mater.* **2019**, *2*, 2161-2168; (b) Y. Tian, X. Hu, Y. Wang, C. Li, X. Wu, *ACS Sustain. Chem. Eng.* **2019**, *7*, 9211-9219; (c) S. Rudra, A. K. Nayak, S. Koley, R. Chakraborty, P. K. Maji, M. Pradhan, *ACS Sustain. Chem. Eng.* **2019**, *7*, 724-733; (d) J. Zhou, C. Zhang, T. Niu, R. Huang, S. Li, J. Z. Zhang, J. G. Chen, *ACS Appl. Energy Mater.* **2018**, *1*, 4599-4605; (e) J. Lin, H. Liang, H. Jia, S. Chen, J. Guo, J. Qi, C. Qu, J. Cao, W. Fei, J. Feng, *J. Mater. Chem. A* **2017**, *5*, 24594-24601.
- [4] S. Bag, C. R. Raj, *J. Mater. Chem. A* **2016**, *4*, 8384-8394.
- [5] S. Yang, Y. Liu, Y. Hao, X. Yang, W. A. Goddard III, X. L. Zhang, B. Cao, *Adv. Sci.* **2018**, *5*, 1700659.
- [6] B. D. Boruah, S. Nandi, A. Misra, *ACS Appl. Energy Mater.* **2018**, *1*, 1567-1574.
- [7] S. Mitra, K. S. Lokesh, S. Sampath, *J. Power Sources* **2008**, *185*, 1544-1549.
- [8] R. Samal, B. Chakraborty, M. Saxena, D. J. Late, C. S. Rout, *ACS Sustain. Chem. Eng.* **2019**, *7*, 2350-2359.
- [9] B. Senthikumar, Z. Khan, S. Park, K. Kim, H. Ko, Y. Kim, *J. Mater. Chem. A* **2015**, *3*, 21553-21561.
- [10] (a) Z. Zhou, Q. Zhang, J. Sun, B. He, J. Guo, Q. Li, C. Li, L. Xie, Y. Yao, *ACS Nano* **2018**, *12*, 9333-9341; (b) A. Samanta, C. R. Raj, *J. Electroanal. Chem.* **2019**, *847*, 113183; (c) D. Moitra, C. Anand, B. K. Ghosh, M. Chandel, N. N. Ghosh, *ACS Appl. Energy Mater.* **2018**, *1*, 464-474; (d) S. Kumar, G. Saeed, N. H. Kim, J. H. Lee, *J. Mater. Chem. A* **2018**, *6*, 7182-7193; (e) R. Kumar, P. Rai, A. Sharma, *J. Mater. Chem. A* **2016**, *4*, 17512-17520.
- [11] X. Chen, K. Chen, H. Wang, D. Xue, *Materials Focus* **2015**, *4*, 78-80.
- [12] B. Zhao, Y. Zheng, F. Ye, X. Deng, X. Xu, M. Liu, Z. Shao, *ACS Appl. Mater. Interfaces* **2015**, *7*, 14446-14455.
- [13] S. Ishaq, M. Moussa, F. Kanwal, M. Ehsan, M. Saleem, T. N. Van, D. Losic, *Sci. Rep.* **2019**, *9*, 5974.
- [14] S. Haghdan, S. Rennecker, G. D. Smith, in *Lignin in Polymer Composites* (Eds.: O. Faruk, M. Sain), William Andrew Publishing, **2016**, pp. 1-11.
- [15] D. Mondal, S. K. Nataraj, A. V. Rami Reddy, K. K. Ghara, P. Maiti, S. C. Upadhyay, P. K. Ghosh, *RSC Advances* **2015**, *5*, 17872-17878.
- [16] E. M. Soliman, S. A. Ahmed, A. A. Fadl, *Arabian Journal of Chemistry* **2011**, *4*, 63-70.
- [17] M. Biswal, A. Banerjee, M. Deo, S. Ogale, *Energy Environ. Sci.* **2013**, *6*, 1249-1259.
- [18] H. Huang, X. Feng, C. Du, S. Wu, W. Song, *Journal of Materials Chemistry A* **2015**, *3*, 4976-4982.
- [19] N. S. McIntyre, D. G. Zetaruk, *Analytical Chemistry* **1977**, *49*, 1521-1529.
- [20] I. N. Shabanova, V. A. Trapeznikov, *Journal of Electron Spectroscopy and Related Phenomena* **1975**, *6*, 297-307.
- [21] Y. Lin, X. Wang, G. Qian, J. J. Watkins, *Chem. Mater.* **2014**, *26*, 2128-2137.
- [22] (a) W. Chen, S. Li, C. Chen, L. Yan, *Adv. Mater.* **2011**, *23*, 5679-5683; (b) S. E. M. Pourhosseini, O. Norouzi, P. Salimi, H. R. Naderi, *ACS Sustain. Chem. Eng.* **2018**, *6*, 4746-4758.
- [23] (a) L. Chen, Z. Kong, S. Yue, J. Liu, J. Deng, Y. Xiao, R. G. Mendes, M. H. Rummeli, L. Peng, L. Fu, *Chem. Mater.* **2015**, *27*, 8230-8236; (b) D. Kondo, K. Yagi, M. Sato, M. Nihei, Y. Awano, S. Sato, N. Yokoyama, *Chem. Phys. Lett.* **2011**, *514*, 294-300; (c) S. Iijima, T. Ichihashi, *Nature* **1993**, *363*, 603-605; (d) S. Fan, M. G. Chapline, N. R. Franklin, T. W. Tomblor, A. M. Cassell, H. Dai, *Science* **1999**, *283*, 512-514; (e) Y. You, M. Yoshimura, S. Cholake, G.-H. Lee, V. Sahajwalla, R. Joshi, *Adv. Mater. Interfaces* **2018**, *5*, 1800599.
- [24] (a) S. Sheng, W. Liu, K. Zhu, K. Cheng, K. Ye, G. Wang, D. Cao, J. Yan, *J. Colloid Interface Sci.* **2019**, *536*, 235-244; (b) X. Zhang, M. Zhu, T. Ouyang, Y. Chen, J. Yan, K. Zhu, K. Ye, G. Wang, K. Cheng, D. Cao, *Chem. Eng. J.* **2019**, *360*, 171-179.
- [25] K. A. Owusu, L. Qu, J. Li, Z. Wang, K. Zhao, C. Yang, K. M. Hercule, C. Lin, C. Shi, Q. Wei, L. Zhou, L. Mai, *Nat. Commun.* **2017**, *8*, 14264.
- [26] (a) S. Mondal, U. Rana, S. Malik, *J. Phys. Chem. C* **2017**, *121*, 7573-7583; (b) S. Zeng, H. Chen, F. Cai, Y. Kang, M. Chen, Q. Li, *J. Mater. Chem. A* **2015**, *3*, 23864-23870.
- [27] H. Khani, D. O. Wipf, *ACS Appl. Mater. Interfaces* **2017**, *9*, 6967-6978.
- [28] H. Zhang, C. Lu, C. Chen, L. Xie, P. Zhou, Q. Kong, *ChemElectroChem* **2017**, *4*, 1990-1996.
- [29] R. Kumar, R. K. Singh, A. R. Vaz, R. Savu, S. A. Moshkalev, *ACS Appl. Mater. Interfaces* **2017**, *9*, 8880-8890.
- [30] M. Saraf, K. Natarajan, Shaikh M. Mobin, *RSC Adv.* **2017**, *7*, 309-317.
- [31] M. Zhi, C. Xiang, J. Li, M. Li, N. Wu, *Nanoscale* **2013**, *5*, 72-88.
- [32] R. Pai, A. Singh, S. Simotwo, V. Kalra, *Adv. Eng. Mater.* **2018**, *20*, 1701116.
- [33] (a) Z. Ma, X. Huang, S. Dou, J. Wu, S. Wang, *J. Phys. Chem. C* **2014**, *118*, 17231-17239; (b) A. Pathak, A. S. Gangan, S. Ratha, B. Chakraborty, C. S. Rout, *J. Phys. Chem. C* **2017**, *121*, 18992-19001.
- [34] Y. Dou, T. Liao, Z. Ma, D. Tian, Q. Liu, F. Xiao, Z. Sun, J. Ho Kim, S. Xue Dou, *Nano Energy* **2016**, *30*, 267-275.

- [35] H. Fan, R. Niu, J. Duan, W. Liu, W. Shen, *ACS Appl. Mater. Interfaces* **2016**, *8*, 19475-19483.
- [36] C. Zequine, C. K. Ranaweera, Z. Wang, P. R. Dvornic, P. K. Kahol, S. Singh, P. Tripathi, O. N. Srivastava, S. Singh, B. K. Gupta, G. Gupta, R. K. Gupta, *Sci. Rep.* **2017**, *7*, 1174.
- [37] Y. Wang, G. Zhang, G. Liu, W. Liu, H. Chen, J. Yang, *RSC Adv.* **2016**, *6*, 44013-44018.
- [38] J. Li, W. Lu, Y. Yan, T.-W. Chou, *J. Mater. Chem. A* **2017**, *5*, 11271-11277.
- [39] A. Mahto, R. Gupta, K. K. Ghara, D. N. Srivastava, P. Maiti, K. D, P.-Z. Rivera, R. Meena, S. K. Nataraj, *J. Hazard. Mater.* **2017**, *340*, 189-201.
- [40] J. W. Choi, I. W. Ock, K.-H. Kim, H. M. Jeong, J. K. Kang, *Adv. Funct. Mater.* **2018**, *28*, 1803695.

